12th International Symposium on Turbulence and Shear Flow Phenomena (TSFP12)
Osaka, Japan, July 19–22, 2022

STATISTICS OF UNSTEADY FAVORABLE PRESSURE GRADIENT TURBULENT BOUNDARY LAYERS

Aadhy Parthasarathy
Aerospace Engineering
University of Illinois at Urbana-Champaign
104 S Wright St, Urbana, Illinois 61801, USA.
aadhysp2@illinois.edu

Theresa Saxton-Fox
Aerospace Engineering
University of Illinois at Urbana-Champaign
104 S Wright St, Urbana, Illinois 61801, USA.
tsaxtonf@illinois.edu

ABSTRACT

The statistics of temporally-strengthening favorable pressure gradient (FPG) turbulent boundary layers (TBLs) are studied, in comparison to corresponding stationary FPG TBLs. The experiments were carried out in a wind tunnel facility capable of imposing unsteady pressure gradients of different timescales on a flat plate TBL through the use of a rapidly deformable ceiling mechanism. The responses of the transient TBL were captured using phase-locked time-resolved particle image velocimetry. A series of steady-state experiments were also performed for 22 discrete states of the ceiling within the deformation range, to help separate the effects of unsteadiness and spatial pressure gradients. The ensemble-averaged mean and Reynolds stresses at a location at the exit of spatial acceleration are presented in this paper, for 3 different timescales of unsteadiness corresponding to reduced frequency, k_x (defined as the ratio of convective timescale to imposed unsteady timescale) = 4.5, 1.5, 0.6. The development of salient features of the steady-state pressure gradient flow and the effect of unsteadiness on these features are discussed. Significant deviations from steady-state behavior are seen for k_x = 4.5 and 1.5, indicating that pseudo-steady assumptions in their numerical simulation using lower-fidelity tools will lead to inaccurate predictions.

INTRODUCTION

Pressure gradient (PG) TBLs are of immense interest to researchers and engineers due to their ubiquitous nature. Increasingly sophisticated experiments (Schröder *et al.*, 2018; Shehzad *et al.*, 2021) and high-fidelity numerical simulations (Piomelli & Yuan, 2013; Gungor *et al.*, 2021) have furnished reliable statistics of favorable and adverse PG TBLs over a large parametric space, allowing lower-fidelity turbulence models to be continually evaluated and improved based on these statistics. Current limitations of these models are well-identified, for example, near flow separation or in sequences of pressure gradients of opposing signs, and these are active areas of research in the turbulence community (Elyasi & Ghaemi, 2019; Slotnick, 2019). Unsteady PG TBLs, on the other hand, have received relatively less attention, despite their practical relevance. Flows over rotating machinery, maneuvering aircraft, and vehicles operating in gusty environments, are some examples. Difficulties in studying these flows range from the complexity in generating unsteady TBLs in a repeatable manner, covering a wide parametric space relevant to engineering situations, to obstacles in meaningfully comparing results from different facilities and simulations (Carr, 1981; Brereton *et al.*, 1990). The current industry standard for full-scale predictions is to use Unsteady Reynolds-Averaged Navier–Stokes (URANS) simulations along with turbulence models for steady PG TBLs, implicitly making the assumption that the unsteady flow is pseudo-steady. Various researchers have shown that such assumptions result in poor predictions due to the effects of complex interactions between the imposed unsteadiness and turbulent fluctuations being absent in these models that are tuned for steady PGs (Park *et al.*, 2021; Rezaeiha *et al.*, 2019).

The focus of this paper is on understanding the effect of unsteady FPGs on the statistics of TBLs in comparison to corresponding statistics of steady FPG TBLs, for different timerates of change of PGs. The goal is to provide insights into key features of unsteady FPG TBLs that can be used to evaluate if lower-fidelity simulations of these flows predict physically consistent features. Additionally, since FPG followed by APG is a common geometric configuration in engineering flows, and considering that history effects play an important role in the dynamics of PG TBLs (Vinuesa *et al.*, 2017), propagating the features of unsteady FPG flows into a succeeding APG region is also of significance in accurately predicting unsteady APG flows.

Accelerated TBLs

A spatially accelerated TBL under FPGs exhibits several interesting features that differ from a ZPG TBL, some of which are reported in Sreenivasan (1982), Bourassa & Thomas (2009), and Dixit & Ramesh (2010). The mean velocity develops an enlarged viscous sublayer and significant deviations from log and wake law behaviors are seen for moderately strong PGs ($K > 2.8 \times 10^{-6}$). The standard-law deviations

mark the onset of relaminarization, a process of reverse transition to laminar flow. The process is triggered by a sufficiently strong suppression of turbulence intensities and of turbulence production, especially in the outer region. A shift in the energy spectrum towards lower wavenumbers is apparent, and the 2-point correlation structures appear elongated and more inclined to the wall. Prolonged application of the FPG can cause the boundary layer to eventually laminarize, but the flow quickly bypass-retransitions to turbulence when the stabilizing effect of the FPG is removed. Turbulence models often fail to predict some features of relaminarizing TBLs, especially pertaining to the behaviors of Reynolds shear stress and turbulent kinetic energy (Saltar & Araya, 2020). More complex dynamics result when the FPG region succeeds an APG, such as in the bump / hill flows of Uzun & Malik (2021), Balin & Jansen (2021), Baskaran *et al.* (1987) that impose a mild APG at the foot of the bump / hill, followed by a strong FPG until the apex. The pressure gradient sign change triggers an internal boundary layer that dominates the near-wall behavior including skin friction, and the Reynolds stress profiles develop footprints of the formation and growth of the internal layer, exhibiting features like knee points and outer peaks that are otherwise absent in FPG flows that succeed a ZPG region.

Literature on temporally-accelerated TBLs is sparse, with most unsteady TBL studies focusing on periodic unsteadiness imposed by means of an oscillatory freestream flow, periodically accelerating and decelerating the boundary layer. Karlsson (1959) imposed sinusoidal oscillations of large amplitudes (upto 34% of the mean) and of a wide range of frequencies (0.33 - 40 Hz) about a constant mean, and reported that the time-averaged mean showed negligible variations compared to the quasi-steady mean, and that the variations in streamwise turbulence intensity were not systematic with frequency and amplitude. Similar experiments by Parikh *et al.* (1981), Menendez & Ramaprian (1989), and Brereton *et al.* (1990) supported the observation of insignificant effects of unsteadiness on time-averaged quantities, but additionally identified strong non-quasi-steady effects when probing the oscillatory (phase-averaged) quantities. Phase leads and lags in the turbulent stresses were noted, and were shown to be a function of the frequency of oscillation. Low frequency oscillations elicited responses throughout the boundary layer, whereas high-frequency oscillations modulated the near-wall most, with the outer region turbulence and the boundary layer thickness remaining effectively frozen at their mean values throughout the cycles. These behaviors were similar in character to that of turbulent pipe and channel flows under periodic unsteadiness.

A non-periodic, rapidly accelerated TBL over a flat plate with non-zero pressure gradients (an FPG-APG sequence imposed by a converging-diverging slip wall) was simulated by Kharghani & PasandidehFard (2022). The effect of temporal acceleration bore similarities to spatially-accelerated flows, resulting in stronger suppression of fluctuations and delays in turbulence propagation due to their simultaneous application. The similarities of temporal acceleration effects to spatial acceleration have previously been noted in rapidly accelerated pipe and channel flows (He & Jackson, 2000; Talha & Chung, 2015). Saavedra & Paniagua (2021) studied the effects of a sudden flow acceleration over a wall-mounted hump (FPG-APG sequence), in the compressible subsonic flow regime. They noted a boost of near-wall momentum due to the sudden acceleration, enough for the TBL to overcome APG-induced flow detachment, suggesting that mean flow transients can be leveraged to modulate separation events. A rapidly accelerated flat plate compressible TBL was studied by Saavedra *et al.* (2020), who saw a significant acceleration effect on the shear stress and heat flux through a sudden overshoot dominated by inertia and a subsequent relaxation to quasi-steady state.

The studies to-date on non-periodic unsteady TBLs have been valuable in the identification of interesting physics and in questioning the adequacy of lower-fidelity simulations. Advancing our understanding of complex mechanisms in these flows and their prediction calls for significantly more research through systematic experiments (physical or numerical) characterizing the unsteady effects over a wide range of parameters relevant to engineering flows of interest. The success of extensive research on rapidly accelerated or decelerated pipe/channel flows serves as additional motivation.

EXPERIMENT

The experiments reported in this paper were performed in an open-return boundary layer wind tunnel at the University of Illinois. Quiescent air is sucked through a 10.19 cm thick honeycomb straightener, followed by four 24-mesh turbulence reducing screens, and a contraction section with an area ratio of 27:1, before reaching a 0.381 m $\times$ 0.381 m $\times$ 3.687 m ($15" \times 15" \times 12'$) test section. The resulting freestream turbulence intensity is approximately 0.5%. A fully-developed TBL is obtained over a 3 m long flat plate with a leading-edge trip, mounted at the test section half-height. The test area was located at 2.3 m from the leading-edge. The zero pressure gradient 99% boundary layer thickness, δ, at the test area was 42 mm and the friction Reynolds number, Re_τ, was 990.

A recently built and characterized installation for the ceiling of the wind tunnel was used to generate the unsteady pressure gradients. A schematic of this installation is shown in Fig.1a. It houses an electro-pneumatic actuation mechanism that rapidly deforms a flexible ceiling panel to the shape of an inverted convex bump. The dimensions of the ceiling panel are 0.45 m $\times$ 0.375 m $\times$ 0.001 m. As the ceiling deforms, a spatially- and temporally-varying favorable and adverse pressure gradient sequence is imposed on the flat plate TBL beneath it. The spatial profile of the PG imposed and the temporal rate at which it is imposed can be varied as desired by providing suitable control inputs to the actuation mechanism. A detailed description of this facility can be found in Parthasarathy & Saxton-Fox (2022).

This paper is focused on studying the temporal response of the TBL at a 1D plane located at x_0 (marked in Fig.1a), where the flow has undergone spatial acceleration whose strength increases with time as the ceiling deforms. The estimated spatial PG profile imposed and its variation in time are shown in Fig.1b over the region $(0 < x/L < 1)$, in terms of the acceleration parameter, K. L is the length of the ceiling panel, and the plane x_0 corresponds to $x/L = 0.5$. K is defined as $\frac{\nu}{U_c^2}\frac{dU_c}{dx}$, where ν is the kinematic viscosity, and U_c is the local bulk velocity. U_c was computed as the bulk velocity variation required to satisfy continuity at all geometric states of the ceiling, and was validated using discrete pressure measurements. The temporal strength or unsteadiness of the PG imposed is quantified in terms of reduced frequency, $k_x = t_c/t_f$, where t_c is the convective timescale and t_f is the imposed unsteady timescale, equal to the ceiling deformation time. k_x = 4.38, 1.53, and 0.61 for the cases discussed in this paper. The convective length and velocity scales used in the definition of k_x are chosen to be the boundary layer development length and freestream velocity, consistent with literature on unsteady pitching airfoil experiments and simulations. A

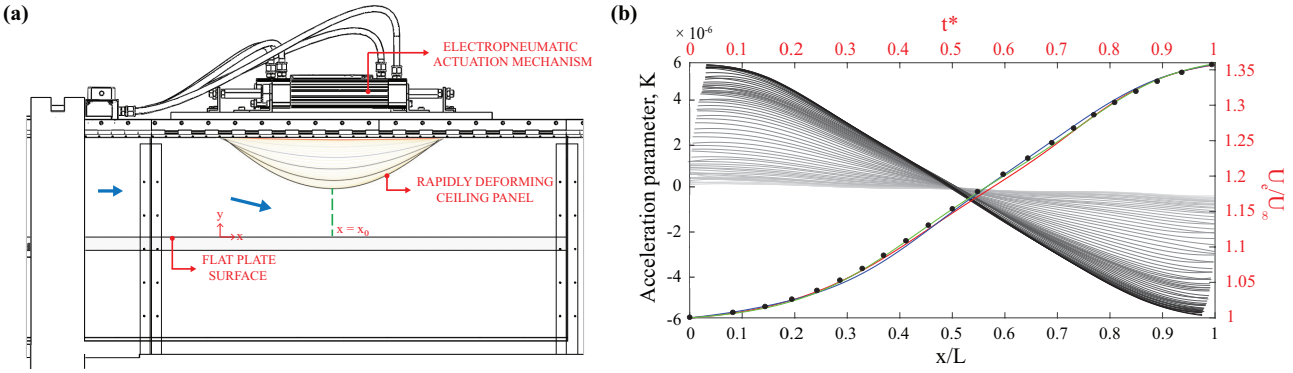

Figure 1. Experimental details. (a) Schematic of unsteady the pressure gradients installation. The geometric states of the ceiling at the 6 instances chosen for analysis in Fig. 2 are shown as gray curves over yellow curves. Flow is from left to right. (b) Left axis : Variation of acceleration parameter in space and in time, where the darker curves indicate later in time. Right axis: Variation of edge velocity in time at location x_0, scaled by freestream velocity (U_∞) and unsteady time (t_f). t_f = 0.07, 0.25, 0.5 s respectively for k1, k2, k3. (——) k1, (——) k2, (——) k3, (•) Steady.

more suitable comparison of the timescales involved in this boundary layer flow is captured by $k_\tau = \tau_t/t_f$, where τ_t is the large turbulent timescale. For the cases discussed, k_τ = 1.79, 0.63, and 0.25, and will be referred to as cases k1, k2, and k3 respectively henceforth.

The time-varying 1D data at x_0 are sourced from a recent experimental campaign to capture the spatio-temporal response of the TBL to unsteady PGs using phase-locked, time-resolved particle image velocimetry at a rate of 3.755 kHz. A mineral-oil based seeding was introduced at the tunnel inlet, and a Continuum®Terra PIV 527-80-M high-speed laser was used along with a Phantom®VEO 710L camera to collect the particle image pairs. For the unsteady cases, 400 independent cycles of the boundary layer response were recorded in a phase-locked manner. Each independent cycle consisted of 280 image pairs for k1, 480 for k2, and 1020 for k3. The number of image pairs per cycle are naturally higher for higher t_f. The resulting vector fields calculated using LaVision's DaVis 10 software had a spatial resolution of $42\delta_v$, where $\delta_v = \nu/u_{\tau_0}$ and u_{τ_0} is the initial zero pressure gradient friction velocity computed using the Clauser method. The temporal resolution was $2\tau_v$, where $\tau_v = \nu/u_{\tau_0^2}$. With 400 phase-locked ensembles, the mean field converged to within 0.1%, the normal Reynolds stresses to within 1%, and the Reynolds shear stress to within 3%. The variation of non-dimensional edge velocity, U_e/U_∞, at x_0 with respect to non-dimensional time, t/t_f, is shown in Fig.1b for each rate of imposition of pressure gradient. The edge velocities and local boundary layer thicknesses used in the outer scaled plots of Fig. 2 and Fig. 3 were calculated using the diagnostic plot technique of Vinuesa *et al.* (2016). For the steady-states, 10,000 velocity fields each were acquired at 0.2 kHz for 22 static configurations of the ceiling.

RESULTS AND DISCUSSION

The ensemble-averaged mean velocity and Reynolds stresses at station x_0 for k1 are shown in Fig. 2 in red for 6 instances in time (t^* = 0, 0.36, 0.53, 0.68, 0.78, 1). The profiles at subsequent t^* are horizontally shifted such that time flows left to right. The corresponding steady-state statistics are plotted in black, showing results from a boundary layer with a static spatial pressure gradient that instantaneously matches that of the time-varying case at time t^*. ZPG profiles at the initial freestream velocity are plotted in grey to highlight differences in the BL response to zero and favorable PGs. At t^* = 0, the ZPG, steady FPG, and unsteady FPG profiles collapse, as expected. The unsteady Reynolds stress profiles are less converged compared to the unsteady mean profiles, but are able to capture the trends in the statistics (validated at t^*=0), permitting their use in interpreting the trends in unsteady behavior ($t^* >$0).

The steady FPG mean velocity profiles, shown in black in Fig. 2a, show the effect of increasingly stronger spatial acceleration on the TBL. The spatial gradient at the final profile shown corresponds to U_e/U_∞ = 1.36 (and t^* = 1 in the unsteady case), as shown in Fig. 1b. The steady FPG profiles are significantly fuller compared to the ZPG profiles as a result of the acceleration. In the unsteady case, as the ceiling deforms, the mean initially overshoots (t^* = 0.36), then undershoots (t^* = 0.68) the corresponding steady-state profiles, before starting to approach the steady-state mean towards the end of the transient (t^* = 1). With the rapid application of the FPG, mass conservation dictates the external flow to immediately accelerate, while the inner boundary layer takes a finite time to negotiate the no slip at the wall. During this initial stage, a large velocity gradient develops near the wall. As time progresses, this inertial effect relaxes through viscous diffusion. This behavior has previously been observed in temporally-accelerating pipe and channel flows (Seddighi *et al.* (2011)), where an initial stage dominated by inertial forces resulted in large velocity gradients near the wall and hence a rapid increase in viscous shear stress, which later relaxed as the frozen turbulence responds to the acceleration, causing the flow to approach steady-state behavior.

The station x_0 is located at the exit of a strong FPG region, immediately followed by a strong APG region. The steady FPG Reynolds stress profiles at x_0, plotted in black in Fig. 2b-d, show many interesting features characteristic of such pressure gradient sign changes. The first is the formation of a knee point in the streamwise Reynolds stress (Fig. 2b) in the third profile (corresponding to the unsteady case t^* = 0.53) at $y/\delta \sim$ 0.23. The knee point is attributed to the formation of an internal layer triggered by the pressure gradient sign change at x_0, as previously observed in bump/hill flows (Baskaran *et al.*, 1987) or when other boundary condition changes occurs. Below this point (sometimes taken as the edge of the internal layer), the streamwise stress peaks, and above, the stress weakens under the effect of the FPG. The presence of the internal layer also causes the formation of outer peaks in the wall-normal (Fig. 2c) and shear stress profiles (Fig. 2d), whose

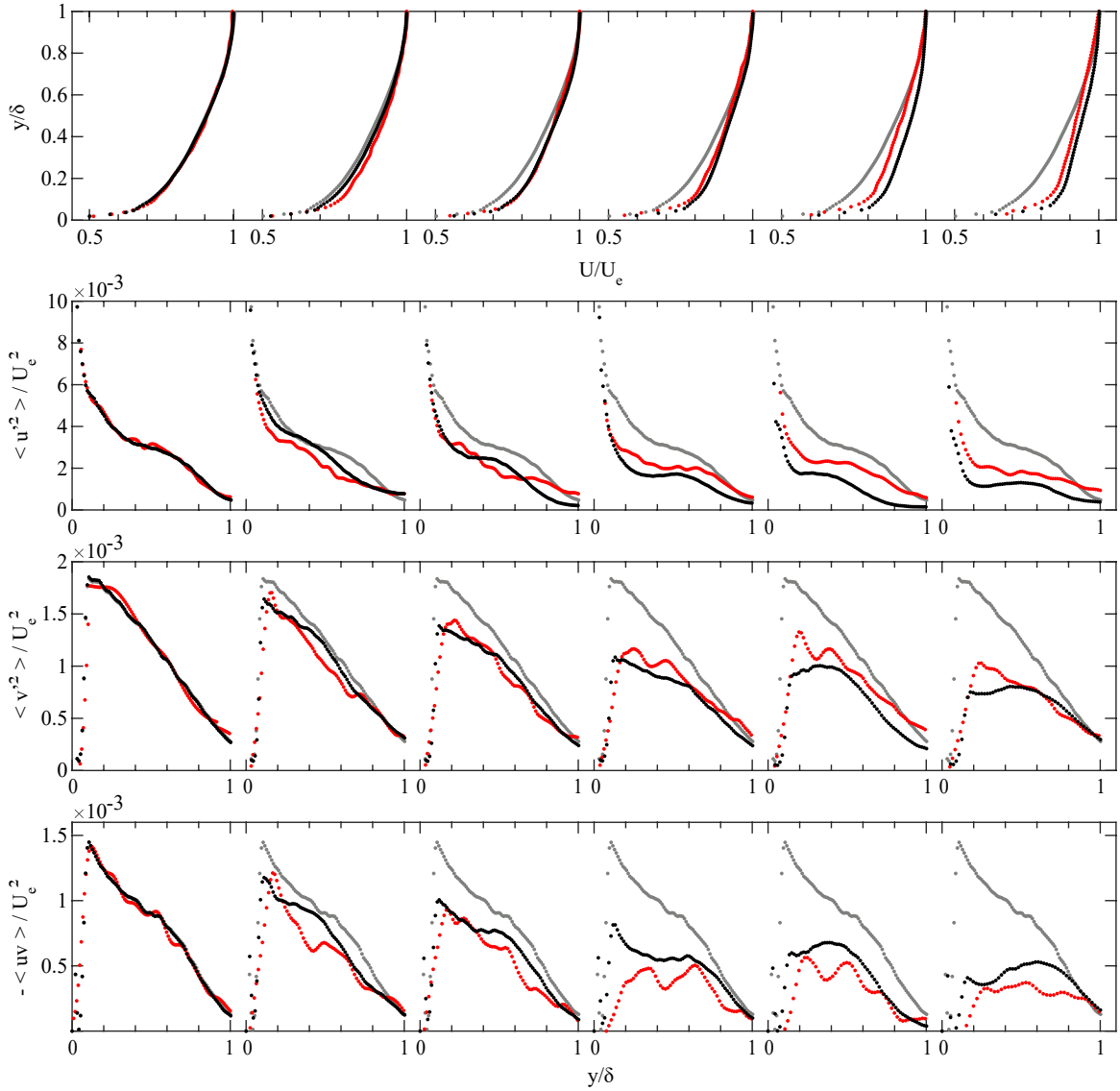

Figure 2. Outer-scaled turbulent statistics at $t^* = 0, 0.36, 0.53, 0.68, 0.78, 1$. (a) Mean streamwise velocity profiles. (b) Streamwise Reynolds stress (c) Wall-normal Reynolds stress (d) Reynolds shear stress. Profiles at subsequent t^* values are shifted by 0.5 units for (a) and 1.1 units for (b), (c), and (d) along the x-axis for visual clarity. (•••) ZPG, (•••) steady FPG , (•••) unsteady FPG.

magnitudes increase with increasing pressure gradient, eventually overtaking the corresponding inner peak magnitudes (evidently visible starting in the fourth profile shown, corresponding to the unsteady cases with $t^* > 0.68$). In the unsteady case, the streamwise stress profiles show an initial rapid suppression in magnitude throughout the boundary layer, causing an overshooting of the corresponding steady profiles, followed by a period of under-response ($t^* > 0.68$). The knee point forms earlier at $t^* = 0.36$ (at a weaker spatial pressure gradient or lower U_e/U_∞ than the steady case), suggesting that the sudden temporal change has aided the mechanism of formation of the internal layer. The depth of the knee point, taken as an indication of how defined/strong the internal layer is, becomes weaker in the unsteady case for $t^* > 0.68$. The unsteady wall-normal and shear stress profiles deviate from the bi-modal structures of the corresponding steady-state responses. The unsteady wall-normal stress exhibits a stronger inner peak and an absence of the outer peak, which can be associated with a weaker internal layer in the unsteady case as the flow evolves. The single shear stress peak shifts further away from the wall compared to the first peak of the corresponding steady-state profile, so that at $t^* = 1$, the unsteady peak is located at $y/\delta = 0.26$, whereas the steady peak is at $y/\delta = 0.16$.

The statistics at discrete time instances in Fig. 2 suggest a significant impact of the unsteadiness on features of the pressure gradient flow, including the formation and wall-normal growth of the internal layer, and the suppression of outer region turbulence. The continuous time behavior of the features discussed is quantified next and the effect of rate of pressure gradient imposition is studied. Fig. 3 shows the temporal evolution of one chosen feature each in the mean and the Reynolds stresses for k1, k2, and k3, along with the variations in the corresponding steady-states. The inset in each figure illustrates the quantity chosen to be tracked in time.

The outer-scaled mean velocity at a point where the mean velocity changes slope is plotted with non-dimensional time in Fig. 3a, to study the over- and under-responses to acceleration seen in Fig. 2a for k1. A similar evolution to k1 is seen in case k2, with the mean velocity overshooting the corresponding steady-state mean for 60% of the unsteady time. The mean velocity undershoots the steady-state for the reminder of unsteady time, and at $t^* = 1$, shows a possibility of reaching

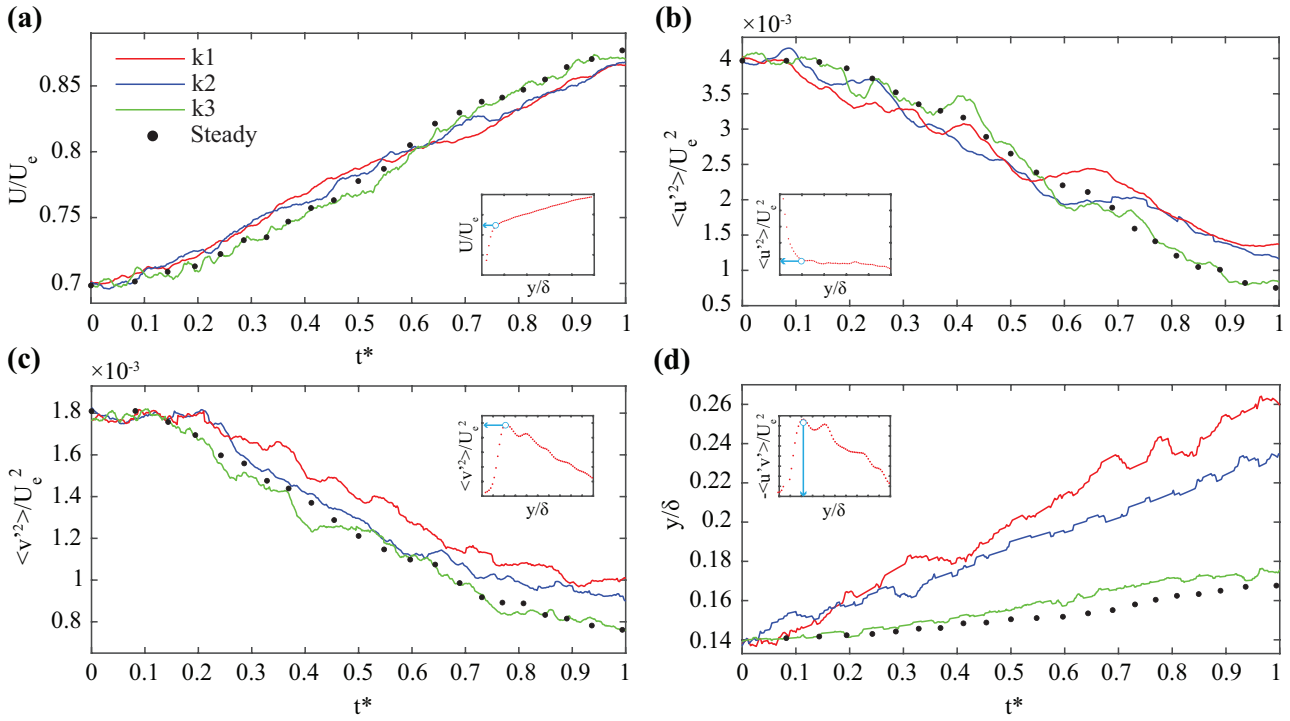

Figure 3. Temporal evolution of select statistical features. (a) Acceleration in the mean. (b) Depth of knee point in the streamwise Reynolds stress. (c) Magnitude of wall-normal Reynolds stress peak. (d) Wall-normal location of Reynolds shear stress peak. The inset in each figure illustrates the definition of the quantity chosen to be tracked in time.

steady-state shortly after. The closest to steady-state behavior is exhibited by case k3, where the temporal evolution of the chosen mean quantity does not exhibit discernible over- or under-responses to the sudden acceleration.

Fig. 3b shows the depth of the knee point in the streamwise Reynolds stress, identified as the first local minimum in the stress profile. The wall-normal location of the knee point (not tracked here) is considered as the edge of the internal layer (Baskaran *et al.* (1987); Efros & Krogstad (2011)). The depth of the knee point is interpreted as indicating how defined/strong the internal layer is, and is tracked here to study the formation of the internal layer in time. Cases k1 and k2 develop an internal layer at $t^* = 0.075$ upon rapid application of the pressure gradient, which persists in a more defined manner than the corresponding steady pressure gradient internal layer upto $t^* = 0.56$ and 0.67 respectively for k1 and k2. After this, the depth of the knee point rises higher than the corresponding steady-state, indicating a weaker internal layer as the boundary layer has negotiated the initial condition change.

The first peak of the wall-normal Reynolds stress profile is tracked in Fig. 3c. Cases k1 and k2 exhibit less suppression of outer-scaled wall-normal stress throughout the unsteady time relative to the steady-states, and more interestingly, show no variation for a significant 20% of unsteady time ($t^* < 0.2$) despite being scaled by the square of an increasing quantity (i.e, U_e^2). Overall, the effects of unsteadiness seem stronger in k1 compared to k2. Similar behavior is observed in Fig. 3d, where the shifting of the wall-normal location of shear stress peak seen in Fig. 2c for k1 is plotted as the y/δ location of the first maxima in time for all cases. k2 exhibits a significant shifting away from the wall, less than k1 and more than k3 and the steady-states. In Fig. 3b-d, case k3 shows the least variation from steady-state behavior.

CONCLUSION

The mean and Reynolds stresses of a flat plate turbulent boundary layer (TBL) encountering unsteady favorable pressure gradients (FPG) of 3 different timescales (reduced frequency, k_x = 4.38, 1.53, 0.61 or k_τ = 1.79, 0.63, 0.25) are studied in this paper, in comparison to the statistics of 22 steady FPG TBLs. The experiments were conducted in a boundary layer wind tunnel facility that employed a rapidly deformable ceiling panel to impose an FPG-APG sequence on a TBL, whose strength increased in time as the ceiling deformed. The time rate of imposition of pressure gradient was varied by suitably prescribing the rate of ceiling deformation. The spatio-temporal response of the TBL was captured using phase-locked, time-resolved particle image velocimetry. The focus of this study was a station x_0 at the exit of the FPG region, where the TBL had encountered temporally-strengthening spatial acceleration.

Outer-scaled statistics in the wall-normal direction for the highest reduced frequency case (k1) at discrete times were presented along with the statistics of corresponding steady-states. The unsteady mean flow comparatively exhibited a significant period of over-response followed by a period of under-response to the imposed rapid acceleration. The development of key features characteristic of steady TBLs at the apex of an FPG-APG sequence, like the formation and growth of an internal layer, and development of outer peaks in the wall-normal and shear stress profiles were discussed. The differences in these characteristic features for the unsteady case k1 were highlighted. The continuous temporal evolution of select features were shown for k1, k2, k3, along with the steady-state responses, to understand the effect of rate of pressure gradient imposition. k3 showed the least deviation from steady-state behavior. k1 (strongest unsteady case with k_τ = 1.79) elicited the most response from the TBL, with significant variations in the Reynolds stresses including a delay in the suppression

of wall-normal stress due to the acceleration and a shift away from the wall of the shear stress peak. The deviations in TBL behavior for k2 were similar to k1, but weaker in comparison.

The similarities of some of the observations to rapidly accelerated pipe and channel flows, which have been studied indetail by the turbulence community, were noted. But as highlighted by PasandidehFard *et al.* (2022), findings on unsteady internal flows cannot be directly applied to external unsteady TBLs. This study contributes to the limited experimental observations on unsteady FPG TBLs over slow, medium, and fast unsteady timescales (relevant to the turbulent timescale, τ_t), highlighting key features of the flow that can potentially be used to test physical consistency of predictions by lower fidelity simulations.

REFERENCES

Balin, Riccardo & Jansen, Kenneth E 2021 Direct numerical simulation of a turbulent boundary layer over a bump with strong pressure gradients. *Journal of Fluid Mechanics* **918**.

Baskaran, V, Smits, AJ & Joubert, PN 1987 A turbulent flow over a curved hill Part 1. Growth of an internal boundary layer. *Journal of Fluid Mechanics* **182**, 47–83.

Bourassa, C & Thomas, FO 2009 An experimental investigation of a highly accelerated turbulent boundary layer. *Journal of Fluid Mechanics* **634**, 359–404.

Brereton, GJ, Reynolds, WC & Jayaraman, R 1990 Response of a turbulent boundary layer to sinusoidal free-stream unsteadiness. *Journal of Fluid Mechanics* **221**, 131–159.

Carr, Lawrence W 1981 A compilation of unsteady turbulent boundary layer experimental data. *Tech. Rep.*. Advisory Group For Aerospace Research and Development Neuilly-Sur-Seine (France).

Dixit, Shivsai Ajit & Ramesh, ON 2010 Large-scale structures in turbulent and reverse-transitional sink flow boundary layers. *Journal of Fluid Mechanics* **649**, 233–273.

Efros, Vladislav & Krogstad, Per-Åge 2011 Development of a turbulent boundary layer after a step from smooth to rough surface. *Experiments in fluids* **51** (6), 1563–1575.

Elyasi, Mohammad & Ghaemi, Sina 2019 Experimental investigation of coherent structures of a three-dimensional separated turbulent boundary layer. *Journal of Fluid Mechanics* **859**, 1–32.

Gungor, Taygun R, Maciel, Yvan & Gungor, Ayse G 2021 Energy transfer mechanisms in adverse pressure gradient turbulent boundary layers. *arXiv preprint arXiv:2112.02980* .

He, S & Jackson, JD 2000 A study of turbulence under conditions of transient flow in a pipe. *Journal of Fluid Mechanics* **408**, 1–38.

Karlsson, Sture KF 1959 An unsteady turbulent boundary layer. *Journal of Fluid Mechanics* **5** (4), 622–636.

Kharghani, M & PasandidehFard, M 2022 Turbulence structures in accelerated flow over a flat plate with non-zero pressure gradient. *Journal of Applied Fluid Mechanics* **15** (2), 311–324.

Menendez, AN & Ramaprian, BR 1989 Experimental study of a periodic turbulent boundary layer in zero mean pressure gradient. *The Aeronautical Journal* **93** (926), 195–206.

Parikh, PG, Reynolds, WC, Jayaraman, R & Carr, LW 1981 Dynamic behavior of an unsteady turbulent boundary layer. In *Unsteady turbulent shear flows*, pp. 35–46. Springer.

Park, Junshin, Ha, Sanghyun & You, Donghyun 2021 On the Unsteady Reynolds-Averaged Navier–Stokes capability of simulating turbulent boundary layers under unsteady adverse pressure gradients. *Physics of Fluids* **33** (6), 065125.

Parthasarathy, Aadhy & Saxton-Fox, Theresa 2022 A novel experimental facility to impose unsteady pressure gradients on turbulent boundary layers. *Experiments in Fluids* **63** (6), 1–14.

PasandidehFard, Mahmoud, Naeimirad, Mohammad *et al.* 2022 Turbulent transient boundary layer over a flat plate. *Ocean Engineering* **244**, 110192.

Piomelli, Ugo & Yuan, Junlin 2013 Numerical simulations of spatially developing, accelerating boundary layers. *Physics of Fluids* **25** (10), 101304.

Rezaeiha, Abdolrahim, Montazeri, Hamid & Blocken, Bert 2019 CFD analysis of dynamic stall on vertical axis wind turbines using Scale-Adaptive Simulation (SAS): Comparison against URANS and hybrid RANS/LES. *Energy Conversion and Management* **196**, 1282–1298.

Saavedra, Jorge & Paniagua, Guillermo 2021 Experimental analysis of Reynolds effect on flow detachment and sudden flow release on a wall-mounted hump. *Experimental Thermal and Fluid Science* **126**, 110398.

Saavedra, J, Poggie, J & Paniagua, G 2020 Response of a turbulent boundary layer to rapid freestream acceleration. *Physics of Fluids* **32** (4), 045105.

Saltar, German & Araya, Guillermo 2020 Reynolds shear stress modeling in turbulent boundary layers subject to very strong favorable pressure gradient. *Computers & Fluids* **202**, 104494.

Schröder, Andreas, Schanz, Daniel, Novara, Matteo, Philipp, Florian, Geisler, Reinhard, Knopp, Tobias, Schroll, Michael & Willert, Christian 2018 Investigation of a high Reynolds number turbulent boundary layer flow with adverse pressure gradients using PIV and 2D-and 3D-Shake-The-Box. In *19th International Symposium on the Application of Laser and Imaging Techniques to Fluid Mechanics*.

Seddighi, Mehdi, He, Shuisheng, Orlandi, Paolo & Vardy, Alan E 2011 A comparative study of turbulence in ramp-up and ramp-down unsteady flows. *Flow, turbulence and combustion* **86** (3-4), 439–454.

Shehzad, Muhammad, Sun, Bihai, Jovic, Daniel, Ostovan, Yasar, Cuvier, Christophe, Foucaut, Jean-Marc, Willert, Christian, Atkinson, Callum & Soria, Julio 2021 Investigation of large scale motions in zero and adverse pressure gradient turbulent boundary layers using high-spatial-resolution particle image velocimetry. *Experimental Thermal and Fluid Science* **129**, 110469.

Slotnick, Jeffrey P 2019 Integrated CFD validation experiments for prediction of turbulent separated flows for subsonic transport aircraft. In *NATO Science and Technology Organization, Meeting Proceedings RDP, STO-MP-AVT*.

Sreenivasan, KR 1982 Laminarescent, relaminarizing and retransitional flows. *Acta Mechanica* **44** (1), 1–48.

Talha, Tariq & Chung, Yongmann M 2015 Large-eddy simulations of temporally accelerating turbulent channel flow. *Journal of Turbulence* **16** (11), 1091–1113.

Uzun, Ali & Malik, Mujeeb R 2021 Simulation of a turbulent flow subjected to favorable and adverse pressure gradients. *Theoretical and Computational Fluid Dynamics* **35** (3), 293–329.

Vinuesa, Ricardo, Bobke, Alexandra, Örlü, Ramis & Schlatter, Philipp 2016 On determining characteristic length scales in pressure-gradient turbulent boundary layers. *Physics of Fluids* **28** (5), 055101.

Vinuesa, Ricardo, Örlü, Ramis, Sanmiguel Vila, Carlos, Ianiro, Andrea, Discetti, Stefano & Schlatter, Philipp 2017 Revisiting history effects in adverse-pressure-gradient turbulent boundary layers. *Flow, turbulence and combustion* **99** (3), 565–587.